de Sagazan, C. and Olive, J.-A., 2021, Assessing the impact of sedimentation on fault spacing at the Andaman Sea spreading center: Geology, v. 49, https://doi.org/10.1130/G48263.1

Data Repository for

# Assessing the impact of sedimentation on fault spacing at the Andaman Sea spreading center

Contents:

- Supplementary Text
- 3 Supplementary Figures (Figures S1, S2 & S3)
- 2 Supplementary Tables (Tables S1 & S2)
- FORTRAN source codes, input files and MATLAB visualization tools
- 6 Animations illustrating key simulations

## SUPPLEMENTARY TEXT

### S1. Extracting fault spacing and *M* from seismic reflection profile PGS08-21

Seismic reflection profile PGS08-21 as interpreted by Jourdain et al. (2016) enables us to measure both fault spacing $\Delta S$ and $M$ at the ASSC. MOR faults typically follow exponential distributions of frequency vs. offset with a characteristic decay length of order 100 m at slow, intermediate, and fast spreading rates (Carbotte and MacDonald, 1994; Cowie et al., 1993; Howell et al., 2016; Shinevar et al., 2019). Thus, smaller faults will inherently be more closely-spaced than larger faults. To compare fault spacing in a manner that minimizes the dependence on fault size, we must target faults with offsets greater or equal to a specified reference value. The exponential nature of the distribution means that faults smaller than the reference size collectively account for much less tectonic strain than the larger faults upon which estimates of spacing and $M$ are based. In this work we focus our analysis on faults with horizontal offsets greater than 100 m, which are resolvable in the seismic profiles of Jourdain et al. (2016), and allow direct comparison with the faults identified by Behn and Ito (2008) and Ito and Behn (2008) in bathymetric data, which all have heaves ≥ 100 m. We added other estimates of fault spacing from different sources in Figure 2 for completeness, but lack details on the smallest offsets that these studies retained (this typically depends on the resolution of the bathymetric dataset).

As illustrated in Figure S1A, we estimate *ΔS* by measuring the horizontal distance between neighboring crustal-scale faults with heaves exceeding 100 m on either side of the axis, at a reference depth of 5 s (two-way travel time). This distance is corrected for the oblique strike of the profile (N-S) relative to the axis-normal direction (N065º, Figure 1A). We do so by multiplying fault spacing measured in the profile by cos(25º). This yields $\Delta S = 8.8 \pm 3$ km at the ASSC.

We followed the method of Escartín et al. (1999) to estimate *M*. We measured fault heaves greater than 100 m along the profile with the help of reflectors highlighted by Jourdain et al. (2016). We were thus able to measure cumulative horizontal tectonic displacement as a function of distance from the axis (Figure S1B). On geological time scales, fault growth and magma emplacement can be approximated as continuous, steady-state processes, hence cumulative tectonic extension vs. distance to the axis should fall on a straight line of slope 1-*M*. Figure S1B shows this for both sides of the axis. Our measurements indicate *M* values between 0.77 and 0.87. It should be noted that we only measured heaves where reflectors could indicate displacement across a fault. Hence we may have missed a minor part of the total tectonic strain, which is why we likely overestimate *M* to some extent. In addition, the obliquity correction applied to the spacing measurements has no bearing on the slope of the line in Figure S2A and was therefore not applied in our estimates of *M*. Finally, while uncertainties in time-to-depth conversions may affect our selection of faults with throws in excess of 100 m, they do not affect estimates of fault heaves, and horizontal distances to the axis or between faults, which are the observables used to determine spacing and *M*.

## S2. Description of the FLAC method

The Fast Lagrangian Analysis of Continua (FLAC, Cundall, 1989) technique is a hybrid finite-element / finite difference method that explicitly solves mass, momentum and heat conservation in a gridded domain representing a 2-D cross-section of a MOR under symmetric extension rate $2U_S$. In this study, we chose a 60-km wide and 20-km deep domain to roughly match the dimensions of the available ASSC data from Jourdain et al. (2016), and set $U_S$ to 19 mm.yr$^{-1}$. The top boundary is free and lithostatic pressure is imposed along the base of the domain.

The code uses a Lagrangian description of the velocity field, with grid nodes being advected at every time step. Thus, the initially regular grid becomes increasingly distorted, which reduces numerical accuracy. In response to this issue, the grid is remeshed whenever a threshold of distortion is reached, that is, when any angle in the grid falls below a critical value. After every remeshing, the values of the stress, strain, temperature and velocity fields are interpolated onto the new grid.

In addition to physical fields, the code also tracks different lithologies via a phase number assigned to every grid element. This is how intrinsic physical properties (density, rheologic parameters… see Table S1) of materials are implemented throughout the domain.

Materials deform according to a dry diabase flow law (Mackwell et al., 1998), which renders them effectively elasto-plastic at temperatures below ~600ºC, and visco-elastic above. In the present work, only density differs from one material to another, rheological parameters are identical. Initial temperature distribution and enhanced diffusive cooling in the center of the domain are chosen so that the brittle lithosphere is ~5 km thick on-axis (Behn and Ito, 2008). This is achieved by multiplying the effective heat diffusivity by a factor of 4 in regions colder than 400ºC and shallower than 4 km. Temperature along the base follows a half-space cooling model with peak temperature of 1300ºC. The sides allow no conductive heat exchange.

Strain localization simulating faults occurs spontaneously in the brittle layer through cohesion loss with accumulated plastic strain when the Mohr-Coulomb criterion is met (e.g., Poliakov and Buck, 1998; Lavier et al., 2000, see Table S1 for parameters). Specifically, cohesion decreases linearly with accumulated plastic strain until it reaches a critical value of 0.25, which roughly translates to 200 m of fault slip. Such a rapid weakening was found to minimize the dependence of fault lifespan on critical strain (Lavier et al., 2000). Magma injection is modeled as a narrow axial "dike" widening at a rate *M* times the full extension velocity (Buck et al., 2005). Diking is accompanied by specific and latent heat injection and elastic stress perturbations, following the approach of Behn and Ito (2008).

**S3. Implementing sedimentation in FLAC**

Starting from the setup of Behn and Ito (2008), we added the possibility of simulating sedimentation (at a rate *s*) on a spreading ridge. Figure S2 illustrates our approach. At every iteration, after the grid has been advected, we begin by vertically extending the topmost elements by a distance $s \times \Delta t$, thus uniformly blanketing the domain. Then, to produce a more realistic representation of a sedimentary layer (e.g., thicker on topographic lows), we apply a diffusion equation to the topography. We tested several diffusion coefficients so as to reproduce topography smoothing by sediments without removing bathymetric features (e.g. axial trough) altogether. We settled for a uniform topographic diffusivity of $10^{-6}$ $m^2.s^{-1}$, which we found appropriate for the range of tectonic uplift rates under consideration (~$cm.yr^{-1}$).

The issue with simply diffusing topography was that this could lead to locally eroding igneous basement, for example in the actively uplifted footwall of a growing fault. To prevent this, we introduced a closely spaced chain of markers that track the initial flat bathymetry as it becomes advected, deformed and buried under sediments. After the first iteration, this chain of markers effectively tracks the sediment-basement interface. This enables us to check that diffusion does not locally bring seafloor topography below this surface (i.e. that the igneous crust is not truncated by “underwater erosion”). When it does, the topography is artificially reset to 10 meters above the sediment-basement interface, with minimal impact on the outcome of simulations.

After several iterations and remeshings due to grid deformation, some elements (i.e., quadrangles contained within 4 nodes) end up entirely above the sediment-basement interface. When this occurs, their phase is changed from “crust” to “sediment”.

## S4. Running the numerical simulations

We include source files for the FLAC model as part of the Data Repository. The folder /source contains the FORTRAN files that need to be compiled to produce an executable "acflac_tracer_sed_diff_track". This is achieved by running the "make_acflac" script. It should be noted that this script may have to be modified according to the FORTRAN compiler available to the user.

Each run from Table S2 can be redone by using the input files listed in folder /input_files. Running a simulation requires the executable and, in the same folder, the hydrother.inp file as well as the corresponding parameter input file "drezina_sXXX_MYYY.inp" renamed as "drezina.inp".

Model outputs can be visualized in MATLAB to create the snapshots shown in Figure 3 by using the functions provided in folder /visualization. Output files (.dat, .rs, .s and .0 files) are necessary to produce model snapshots and must be found by the MATLAB functions, either by copying them in the same directory or by using the "addpath" command.

Note that in order to start a new simulation from the beginning, output files must be removed from the directory of the executable. Otherwise, the simulation restarts from where it last stopped.

## S5. Note on the animations

We include in the supplement six videos in *.avi* format, corresponding to sedimentation rates of 0, 0.5 and 1 mm.yr$^{-1}$, and to $M$ of 0.6 and 0.8. They display a map of plastic strain throughout the 5-Myr long simulations. The values of $M$ and $s$ are specified in the file names (for example *video_S1.00_M0.80.avi* corresponds to $s$ = 1 mm.yr$^{-1}$ and $M$ = 0.8.). We note an odd event at the very end of *video_S0.50_M0.80.avi*: a few frames before the end of the simulation, faulting stops and tectonic deformation focuses on the central area. Since it occurs only on this particular run, and right before the end, thus not affecting our results, we attribute it to a numerical artifact.

## SUPPLEMENTARY REFERENCES


Carbotte, S. M., and K. C. Macdonald (1994), Comparison of seafloor tectonic fabric at intermediate, fast, and super fast spreading ridges: Influence of spreading rate, plate motions, and ridge segmentation on fault patterns, J. Geophys. Res., 99, 609–613.

Cowie, P. A., C. H. Scholz, M. Edwards, and A. Malinverno (1993), Fault strain and seismic coupling on mid-ocean ridges, J. Geophys. Res., 98, 911–917.

Howell, S. M., Ito, G., Behn, M. D., Martinez, F., Olive, J. A., & Escartín, J. (2016). Magmatic and tectonic extension at the Chile Ridge: Evidence for mantle controls on ridge segmentation. Geochemistry, Geophysics, Geosystems, 17(6), 2354-2373.

Shinevar, W., Mark, H., Clerc, F., Codillo, E., Gong, J., Olive, J.-A., Brown, S., Smalls, P., Liao, Y., LeRoux, V., and Behn, M. D., Causes of oceanic crustal thickness oscillations along a 74-Myr Mid-Atlantic Ridge flow line, *Geochem. Geophys. Geosyst.*, 20, 2019.


## SUPPLEMENTARY FIGURE CAPTIONS

**Figure S1.** Measuring fault spacing and *M* in profile PGS08-21 from Jourdain et al. (2016). **A:** Measuring spacing (reproduced and modified from Jourdain et al., 2016). Red line shows the 5 s mark on the two-way travel time axis. Yellow diamonds indicate points between which spacing was measured. **B:** Measuring *M*. Circles correspond to individual faults (e.g., on either side the heave of fault *N* is the vertical distance between circle *N* and circle *N*-1). Lines are linear regression fits, with slope corresponding to 1-*M* (Escartín et al., 1999).

**Figure S2.** Implementing sedimentation in the FLAC method. Blue line represents the seafloor at all times during the run. Yellow line represents the initial seafloor. As it progressively gets advected and buried throughout the run, it represents the sediment-basement interface.

**Figure S3.** Fault spacing as a function of lifespan for model runs. Each point represents mean spacing and lifespan for a given run. Colors indicate $M$, symbols indicate sedimentation rate $s$. Dots: no sedimentation. Stars: $s$ = 0.25 mm.yr$^{-1}$. Circles: $s$ = 0.50 mm.yr$^{-1}$. Triangles: $s$ = 0.75 mm.yr$^{-1}$. Squares: $s$ = 1.00 mm.yr$^{-1}$. Lines are the relationships between spacing and lifespan proposed by Buck et al. (2005) in their simple kinematic model (see Equation (1) in main text).

**Table S1.** Summary of key input parameters. In the input files provided as part of the supplementary material, all parameters are in international system units, unless specified otherwise. In particular, velocities are in m.s$^{-1}$ and not in mm.yr$^{-1}$.

[a]In each input file, the parameter for each phase is not density itself but density difference with respect to water (e.g. the input parameter for mantle density is not 3300 kg.m$^{-3}$ but 2300 kg.m$^{-3}$).

**Table S2.** Summary of model results.

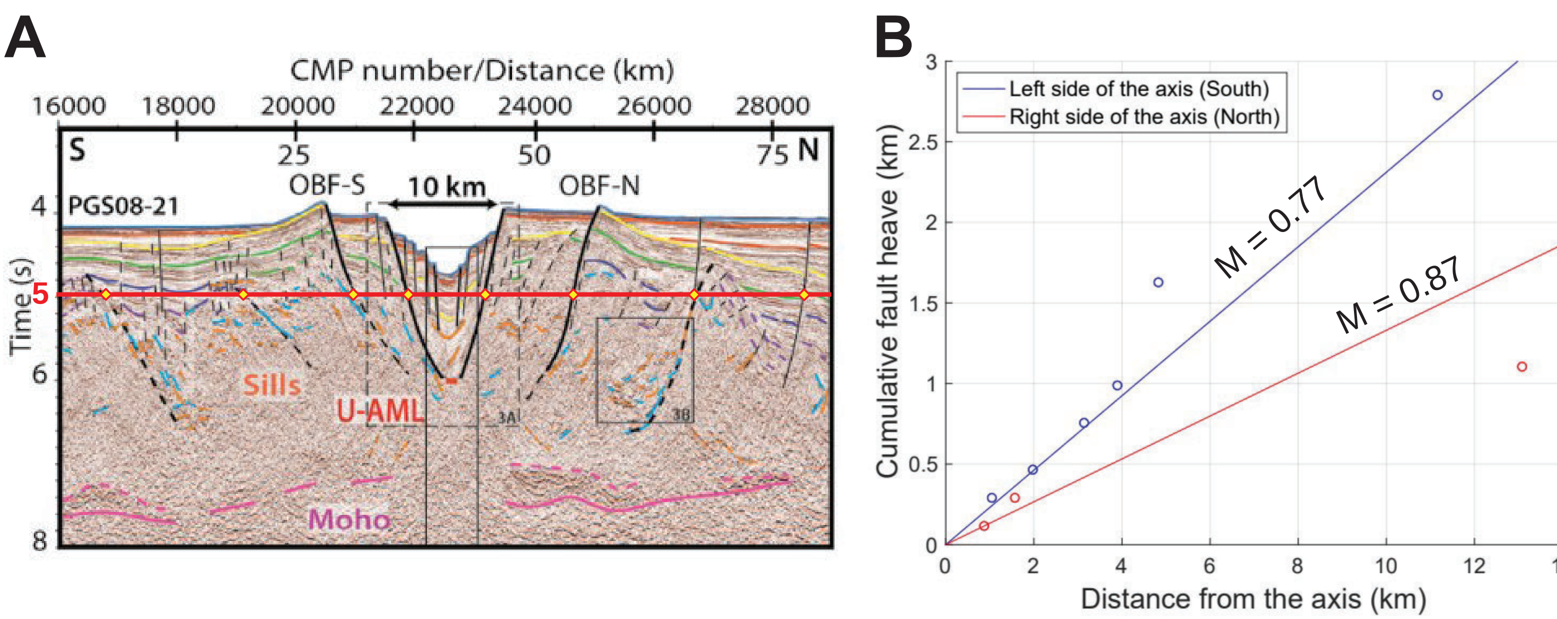
A
CMP number/Distance (km)
16000
18000
20000
22000
24000
26000
28000
S
25
50
75
N
PGS08-21
OBF-S
10 km
OBF-N
Time (s)
4
5
6
8
Sills
U-AML
Moho
3A
3B
B
Left side of the axis (South)
Right side of the axis (North)
M = 0.77
M = 0.87
Cumulative fault heave (km)
Distance from the axis (km)
0
0.5
1
1.5
2
2.5
3
0
2
4
6
8
10
12
14

Figure S1

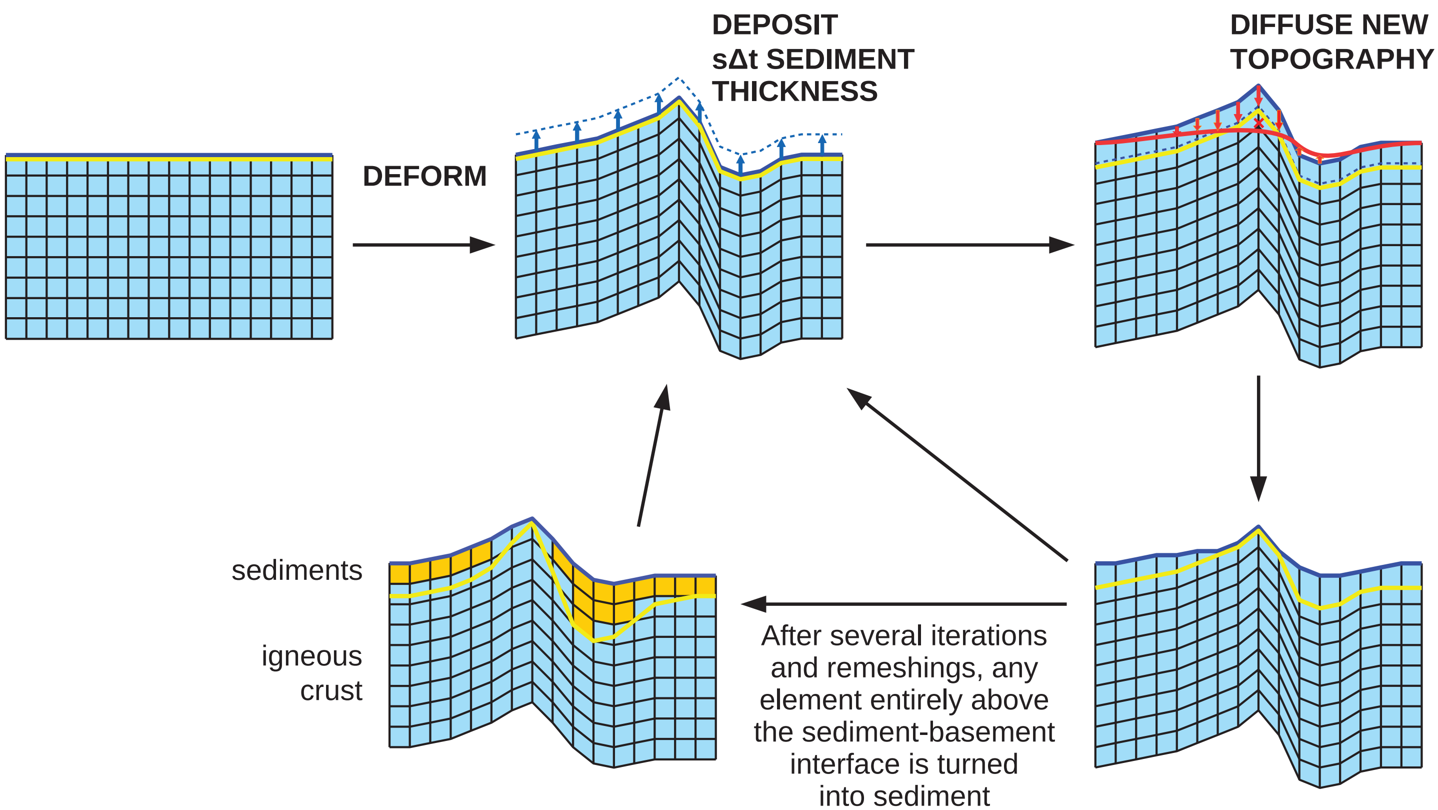
DEFORM
DEPOSIT
sΔt SEDIMENT
THICKNESS
DIFFUSE NEW
TOPOGRAPHY
sediments
igneous
crust
After several iterations
and remeshings, any
element entirely above
the sediment-basement
interface is turned
into sediment

Figure S2

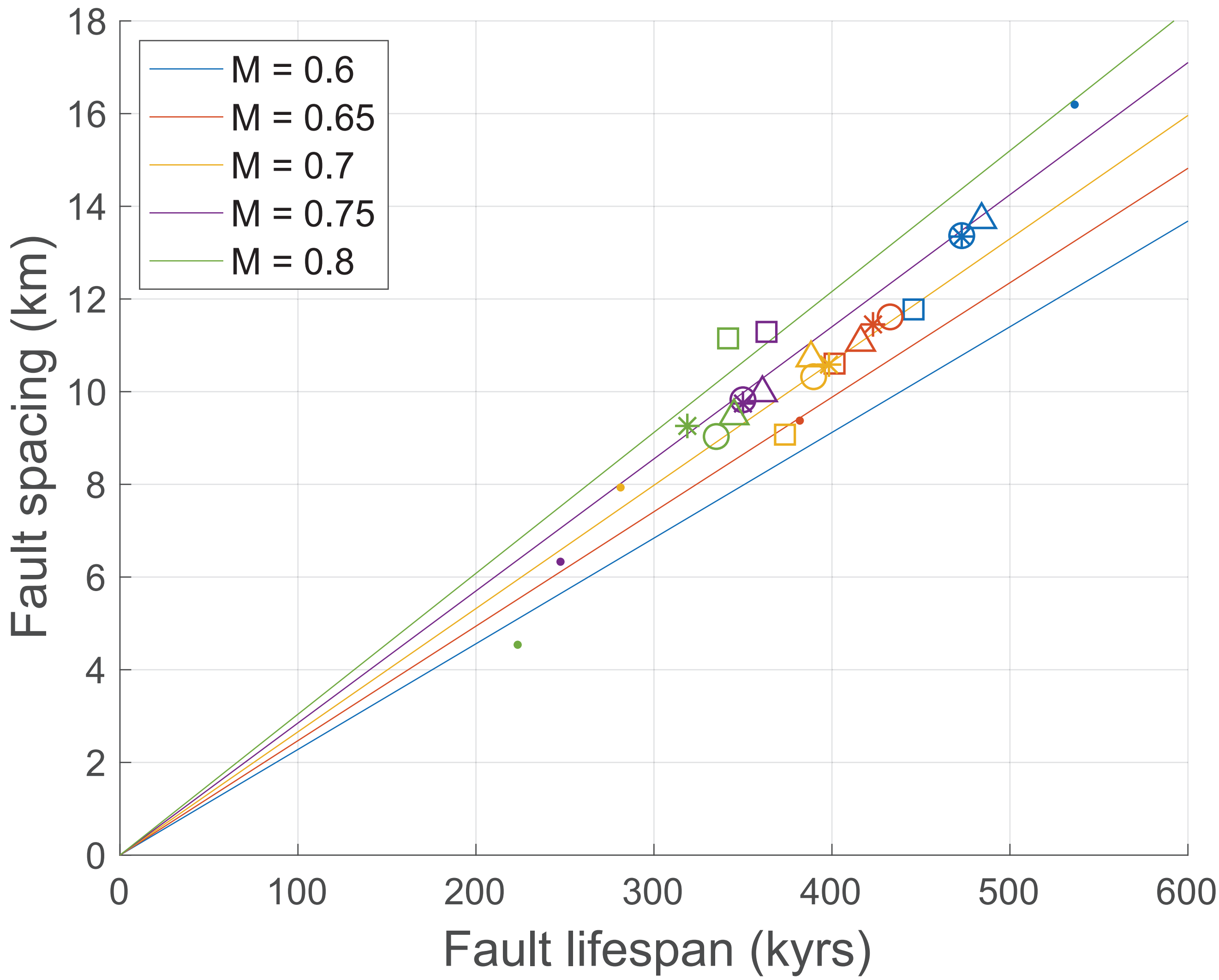

M = 0.6
M = 0.65
M = 0.7
M = 0.75
M = 0.8
Fault spacing (km)
Fault lifespan (kyrs)
0
2
4
6
8
10
12
14
16
18
0
100
200
300
400
500
600


Figure S3